Monte Carlo radiative transfer for the nebular phase of Type Ia supernovae

L. J. Shingles [ORCID],[1]* S. A. Sim,[1] M. Kromer [ORCID],[2,3] K. Maguire [ORCID],[1] M. Bulla [ORCID],[4,5] C. Collins,[1] C. P. Ballance,[6] A. S. Michel,[2] C. A. Ramsbottom,[6] F. K. Röpke,[2,3] I. R. Seitenzahl [ORCID][7] and N. B. Tyndall[6]

[1]*Astrophysics Research Center, School of Mathematics and Physics, Queen's University Belfast, Belfast BT7 1NN, UK*
[2]*Zentrum für Astronomie der Universität Heidelberg, Institut für Theoretische Astrophysik, Philosophenweg 12, D-69120 Heidelberg, Germany*
[3]*Heidelberger Institut für Theoretische Studien, Schloss-Wolfsbrunnenweg 35, D-69118 Heidelberg, Germany*
[4]*Oskar Klein Centre, Department of Physics, Stockholm University, SE-106 91 Stockholm, Sweden*
[5]*Nordita, KTH Royal Institute of Technology and Stockholm University, Roslagstullsbacken 23, SE-106 91 Stockholm, Sweden*
[6]*Centre for Theoretical Atomic, Molecular and Optical Physics, School of Mathematics and Physics, Queen's University Belfast, Belfast BT7 1NN, UK*
[7]*School of Science, University of New South Wales, Australian Defence Force Academy, Canberra, ACT 2600, Australia*

ABSTRACT

We extend the range of validity of the ARTIS 3D radiative transfer code up to hundreds of days after explosion, when Type Ia supernovae (SNe Ia) are in their nebular phase. To achieve this, we add a non-local thermodynamic equilibrium population and ionization solver, a new multifrequency radiation field model, and a new atomic data set with forbidden transitions. We treat collisions with non-thermal leptons resulting from nuclear decays to account for their contribution to excitation, ionization, and heating. We validate our method with a variety of tests including comparing our synthetic nebular spectra for the well-known one-dimensional W7 model with the results of other studies. As an illustrative application of the code, we present synthetic nebular spectra for the detonation of a sub-Chandrasekhar white dwarf (WD) in which the possible effects of gravitational settling of ^{22}Ne prior to explosion have been explored. Specifically, we compare synthetic nebular spectra for a 1.06 $M_\odot$ WD model obtained when 5.5 Gyr of very efficient settling is assumed to a similar model without settling. We find that this degree of ^{22}Ne settling has only a modest effect on the resulting nebular spectra due to increased ^{58}Ni abundance. Due to the high ionization in sub-Chandrasekhar models, the nebular [Ni II] emission remains negligible, while the [Ni III] line strengths are increased and the overall ionization balance is slightly lowered in the model with ^{22}Ne settling. In common with previous studies of sub-Chandrasekhar models at nebular epochs, these models overproduce [Fe III] emission relative to [Fe II] in comparison to observations of normal SNe Ia.

Key words: atomic processes – line: formation – radiative transfer – methods: numerical – supernovae: general – white dwarfs.

1 INTRODUCTION

Type Ia supernovae (hereafter SNe Ia) have proven extremely valuable for cosmology as standardizable candles that enable measurement of the expansion history of the Universe (Riess et al. 1998; Perlmutter et al. 1999). SNe Ia are also a major source of Fe-group elements that are a crucial ingredient for galactic chemical evolution (Nomoto, Thielemann & Yokoi 1984; Matteucci & Greggio 1986). The broad consensus is that SNe Ia involve the thermonuclear destruction of an electron-degenerate white dwarf (WD; Hoyle & Fowler 1960; Bloom et al. 2012), with their extremely high peak brightness and subsequent decline powered by the radioactive decay of ^{56}Ni produced in the explosion (Arnett 1979). However, despite decades of observational and theoretical studies (for a review, see e.g. Hillebrandt et al. 2013), even the most typical SN Ia events are still poorly understood at a fundamental level, with no conclusive determination of either the progenitor systems or the mechanism by which they explode. A recent review of explosion models is given by Livio & Mazzali (2018).

A natural candidate for triggering the ignition is for the WD to approach the Chandrasekhar mass (M_{ch}) limit by accretion

from a companion star. A near-M_{ch} C–O WD that undergoes a pure detonation would result in a composition of mostly Fe-group elements (Arnett 1969; Hansen & Wheeler 1969), which would fail to explain the observed lines of intermediate-mass elements such as silicon and sulphur in SN Ia spectra. Alternatively, a deflagration, which proceeds sub-sonically, would allow the stellar material to expand ahead of the flame front and reduce the densities at which the burning takes place. Although pure-deflagration models produce intermediate-mass elements, self-consistent three-dimensional models (e.g. Fink et al. 2014) fail to match the spectral features and high luminosities observed in normal SNe Ia. The limitations of these two extremes have motivated M_{ch} models with a delayed detonation: a detonation that is preceded by a pre-expansion phase due to subsonic deflagration burning (Khokhlov 1991). For recent multi-D realizations of this model, see e.g. Kasen, Röpke & Woosley (2009) and Seitenzahl et al. (2013).

Another way for nuclear burning to take place at lower densities is for the detonation to occur in a WD with a mass below the Chandrasekhar mass limit (a sub-M_{ch} explosion). Finding a trigger for the explosion has proved challenging, although a promising explanation is that accretion from a companion triggers a surface detonation in a thin He-shell, which then leads to a second detonation of the C–O core (the double-detonation scenario; Livne 1990; Livne & Glasner 1990).

One difficulty in determining the progenitor systems and explosion mechanisms of SNe Ia is that a variety of distinct scenarios lead to very similar predictions for the observable light curves and spectra. For example, Röpke et al. (2012) compared observations of the well-studied SN2011fe with two different explosion models, the N100 DDT (deflagration-to-detonation transition) model by Seitenzahl et al. (2013) and a model of a violent merger between 1.1 and 0.9 $M_\odot$ WDs (Pakmor et al. 2012). For at least the first 30 d, the light curves and spectra calculated for the two explosion scenarios both produced a reasonable fit to the observations, with neither being clearly excluded nor favoured by the data.

A promising resolution to the degeneracy between scenarios is to observe supernovae at very late times, when they have reached their nebular phase and become optically thin at most wavelengths. In SNe Ia, the transition to a nebular phase occurs around several tens of days after explosion, after which photons emitted by the gas typically escape rather than being reabsorbed by the ejecta. Under these conditions, excitation by both radiative and collisional processes are slow, and only lowest energy states have significant populations. The spectra of nebular-phase SNe Ia are therefore dominated by forbidden line emission from the lowest lying metastable states of Fe, Co, and Ni (Spyromilio et al. 1992).

A consequence of the direct relationship between velocity and radius under homologous expansion is that nebular emission lines and their Doppler shifts reveal the distribution of emitting gas throughout the entire ejecta (for a review, see Jerkstrand 2017). This includes the inner core where ignition has taken place and for which some simulations predict an asymmetric three-dimensional structure, dependent on the degree of mixing that has taken place following ignition and prior to the homologous expansion phase. For example, detections of double-peaked line profiles of Fe and Co in nebular-phase spectra have been claimed (Dong et al. 2015), suggesting that explosions result in bimodally structured ejecta (see also Mazzali et al. 2018).

The first models of the SN Ia nebular phase were the one-zone models of Axelrod (1980), who applied a simplified treatment of gamma-ray absorption and a high-energy limit approximation to non-thermal ionization and heating processes. Since the work of

Axelrod (1980), SNe Ia nebular studies have advanced to multizone models with more detailed treatment of gamma-ray transfer, radiative processes, and non-thermal physics (Ruiz-Lapuente & Lucy 1992; Liu, Jeffery & Schultz 1997; Mazzali et al. 2001; Höflich et al. 2004; Kozma et al. 2005; Li, Hillier & Dessart 2012; Botyánszki & Kasen 2017). Such studies have demonstrated the power of nebular-phase observations to constrain key properties of the inner ejecta and test the accuracy with which different explosion scenarios can reproduce composition, ionization, and thermal profiles consistent with observations.

However, despite the effectiveness of late-time spectra in constraining the composition and geometry of the inner ejecta, full three-dimensional radiative transfer simulations for state-of-the-art SNe Ia explosion models in the nebular phase are rare in the literature: many existing studies that depart from spherical symmetry are based on simplified toy geometries (e.g. Maeda et al. 2010) or superposition of 1D models (e.g. Mazzali et al. 2018) and/or assume optically thin emission (e.g. Botyánszki, Kasen & Plewa 2018).

Our aim is therefore to develop and present numerical spectrum synthesis for sets of modern, multi-D explosion simulations in order that they can be used to constrain explosion theories. Accordingly, in this paper, we present extensions to the 3D Monte Carlo radiative transfer code ARTIS in order to extend its validity to the modelling of the nebular phase.

2 NUMERICAL METHOD

We model radiative transfer in SNe Ia using the ARTIS code described by Sim (2007) and Kromer & Sim (2009) (see also Lucy 2005, for a description of the method). ARTIS is a three-dimensional Monte Carlo radiative transfer code that uses indivisible energy packets (Lucy 2002). The code has been extended to trace polarization by Bulla, Sim & Kromer (2015). Here, we describe further developments to the code to extend its validity into the nebular epoch.

The ARTIS code solves for the plasma conditions at each time-step by neglecting time-dependent terms and assuming that the plasma is in statistical, thermal, and ionization equilibrium. These conditions imply equilibrium level populations (as rates into and out of each level are balanced), equilibrium electron temperature (as heating is balanced by cooling, provided a solution falls within the allowed temperature range), and equilibrium ionization balance (as recombination is balanced by ionization), respectively.

The steady-state assumption has been shown to remain valid for supernovae well into the nebular phase to very late times after the explosion. In the Type II supernova SN1987A, Fransson & Kozma (1993) detected a freeze-out of the ionization state due to slowing of ionization and recombination at around ∼800 d. More relevant for our study of SNe Ia are the radiative transfer models of SN2011fe by Fransson & Jerkstrand (2015). Their comparison between a steady-state model and one in which time-dependent effects have been included shows that the time dependence starts to become important at around ∼700 d after explosion. With these results as a guide, we limit our use of the ARTIS code to times earlier than ∼700 d at which the steady-state assumption is a reasonable approximation.

2.1 New atomic data set

Prior calculations with ARTIS have used the 'big_gf-4' atomic data set described by Kromer & Sim (2009), with transition line data from Kurucz & Bell (1995) and Kurucz (2006). This earlier atomic data set did not include sufficiently complete data (such as electron

collision and radiative transition rates) to accurately treat forbidden transitions. However, the nebular spectra of SNe Ia are dominated by forbidden lines, and therefore we have adopted a new atomic data set for use in the studies presented here.

Our data set is based on the atomic data compilation of CMFGEN[1] (Hillier 1990; Hillier & Miller 1998), with some modifications described below. Our standard models in this work include C I–IV, O I–IV, Ne I–III, Mg I–II, Si I–IV, S I–IV, Ar I–IV, Ca I–IV, Fe I–V, Co II–IV, and Ni II–V.

Energy levels in the CMFGEN compilation are generally sourced from Kurucz & Bell (1995), Kurucz (2006), and the NIST Atomic Spectra Database.[2] The photoionization cross-sections are sourced from the Opacity Project (Seaton 1987) and the Fe project (Hummer et al. 1993), which is also a source of electron collisional data. Forbidden line data is sourced from Quinet & Le Dourneuf (1996) for Ni II, Garstang (1958) for Ni III, Quinet, Le Dourneuf & Zeippen (1996) for Fe II, and Quinet (1996) for Fe III.

Our photoionization cross-sections are scaled such that the total recombination rate of each ion when LTE level populations at 6000 K are assumed exactly matches the tabulated recombination rates of Nahar (Nahar & Pradhan 1994; Nahar 1996, 1997; Nahar, Bautista & Pradhan 1997; Nahar, Bautista & Pradhan 1998; Nahar & Bautista 2001) for Fe and Ni^{2+}, and CHIANTI (Dere et al. 1997; Del Zanna et al. 2015) for all other elements/ions. The recombination rate coefficients of the individual levels (derived from the photoionization cross-sections by the Milne relation) are then applied to the specific non-LTE populations during the simulation. The use of non-LTE populations has a very small effect on the ion-recombination rates, since recombination typically proceeds from states in the ground multiplet, which remain close to their LTE populations. The CHIANTI recombination rates for Co ions are obtained by adding fits to the radiative rate from Landini & Fossi (1991) to a fitted dielectronic recombination rate from Mazzotta et al. (1998).

In addition to the CMFGEN data base, we use updated collision strengths for Co$^+$ from Storey, Zeippen & Sochi (2016), and Co$^+$ photoionization cross-sections, Co^{2+} energy levels and bound–bound transition rates from Tyndall et al. (2016).

To calculate bound–bound collisional transition rates, we apply effective collision strengths for the typical electron temperature ($\sim 6 \times 10^3$ K) where this data is available (e.g. Co$^+$ and most ions in the CMFGEN compilation including Fe^{0+}–Fe^{3+}). For collision strengths that are specified only between LS terms without J-splitting (such as Ni^{2+} data by Watts & Burke 1999), we apply the collisional strength to each relevant pair of J-specific levels with a factor accounting for the fraction of statistical weight in the J-specific upper level relative to the total statistical weight of the upper term. Collisional rates for radiatively permitted transitions without effective collision strengths are estimated with the van Regemorter (1962) approximation. For forbidden transitions without collision strengths in the data base, we adopt an effective collision strength of $\Upsilon_{jk} = 0.01 g_j g_k$ where g_j and g_k are the statistical weights of the lower and upper levels (similar to Axelrod 1980). Despite these improvements, it should be noted that the accuracy of high-quality simulations is limited by the quality of the atomic data. In particular, more-complete sets of collision strengths (e.g. for Fe^{3+} and higher, and Co) and improvements to the photoionization cross-sections are priorities for future work.

2.2 Radiation field and photoionization estimators

To calculate the rates of radiative excitation, photoionization, and bound-free heating, the most accurate technique is to directly count the contribution along every Monte Carlo packet flight path. However, this requires storing a rate estimator for each atomic process in every grid cell (or alternatively, storing the full history of all packets), which does not easily scale to the large grid sizes of 3D models. Consequently, we prioritize accurate treatment of photoionization, and currently adopt a radiation field model for other atomic processes (see below).

2.2.1 Photoionization estimators

We use the full packet trajectories to obtain estimators for all photoionization transitions (using equation 44 of Lucy 2003). This provides detailed level by level photoionization rate coefficients, which are then used in our NLTE solution (Section 2.3).

2.2.2 Bound–bound and heating estimators

To estimate rate coefficients for bound–bound process (as required for our NLTE solution – see Section 2.3) and radiative heating rates, we construct a radiation field model in each grid cell.

In prior versions of the ARTIS code, the radiation field in each grid cell is modelled as a dilute blackbody described by two parameters: the radiation temperature T_R and the dilution factor W, by which the radiation field has been weakened relative to the Planck function. The radiation temperature is chosen such that the mean frequency of the Planck function is equal to the energy-weighted mean frequency of the propagating packets (Mazzali & Lucy 1993, also used by Long & Knigge 2002). The dilution factor is then used to scale the blackbody field to the required energy density. The mean intensity and frequency moments are obtained from estimators calculated with the packet trajectory summation technique described by Lucy (1999).

In the nebular epoch, however, the radiation field within the SN Ia ejecta will deviate substantially from a blackbody, and so we require a more detailed treatment of the radiation field. To achieve this with reasonable memory requirements, we accumulate the mean intensity J and the moment νJ_ν estimators independently within each of a set of frequency bands. Specifically, for each segment of a packet trajectory, we calculate a contribution to the J_i and νJ_i estimators of frequency band i that contains the packet's co-moving frequency ν, i.e.

$$\Delta J_i = \frac{\Delta r \, n h \nu}{\Delta V \Delta t},\tag{1}$$

$$\Delta(\nu J_i) = \nu \Delta J_i,\tag{2}$$

where Δr is the distance travelled by a packet representing n photons with co-moving frequency ν during the time Δt in a grid cell with a volume of ΔV. The ratio of νJ_ν to J_ν gives the intensity-weighted mean photon frequency ($\bar{\nu}$) for the frequency band. We then assign to the band a radiation temperature, $T_{R,i}$, obtained by iteratively searching for a temperature in the range 500 to 250 000 K such that the windowed Planck function has the closest matching $\bar{\nu}$ to the estimator value. A dilution factor W_i is then calculated to scale the intensity of the windowed Planck function to the estimator value. A similar binning approach was adopted by the Monte Carlo code of Higginbottom et al. (2013).

In this work, we fit dilute blackbody functions to 255 bins from 1085 to 40 000 Å. 1085 Å has been chosen to ensure that

---

recombination to the highest metastable level of Fe$^+$ has a threshold frequency outside the bins. Short-ward of 1085 Å (where packet statistics are limited and opacities are relatively high), we adopt the local electron temperature for the radiation field but impose a scaling factor to enforce energy conservation.

With the radiation field model obtained in this way, we can then estimate bound–bound radiative rates using equation 10 of Lucy ([2003](#)) with the blue-wing mean intensity estimated from the appropriate bin of the radiation field model. This approach is clearly less accurate that using detailed line-by-line estimators (i.e. equation 46 of Lucy [2003](#)) however it is substantially less demanding of memory requirements and, as discussed by (Kerzendorf & Sim [2014](#), see their fig 14), adopting mean intensities from a radiation field model will often provide a good estimate. We also use the radiation field model to determine bound–free heating rates for use in our calculation but we note that heating via non-thermal deposition is always dominant in the calculations we discuss here.

2.3 Non-LTE ionization and population solver

We calculate the ionization balance and level populations by solving the equations of statistical equilibrium for each grid cell and time-step. For each element, we solve for the populations of all non-local thermodynamic equilibrium (NLTE) energy levels of all included ionization stages simultaneously. The simultaneous whole-element solution enables the easy implementation of multiple ionizations from the non-thermal solver (Section 2.4).

In matrix form, the statistical balance equations are written

$$\sum_{j \neq k} n_j R_{j \to k} - n_k \left(\sum_{j \neq k} R_{k \to j} \right) = 0 \tag{3}$$

for each pair of levels j and k, where n_j and n_k are the populations of level j and k, and $R_{j \to k}$ is the total rate per population of all processes that remove population from level j and add it to level k.

Treating all levels of all ions in NLTE has a large memory and computational cost, so we restrict the number of levels treated in full NLTE. With the first l levels treated in full NLTE, we combine the population of the levels $l + 1 \ldots l_{max}$ into a 'superlevel' (Anderson [1989](#)). While the superlevel is treated as an additional NLTE level that can vary in population, the ratios between the populations of the levels that comprise it are calculated with the assumption that these levels are in Boltzmann equilibrium with each other at the electron temperature. For most ions, we treat the first 80 levels in NLTE, but increase this to 197 NLTE levels for Fe$^+$ to ensure coverage of all metastable levels (those with no permitted transitions to the ground state).

The processes contributing to the rate equation include excitation and de-excitation by radiation and collisions with thermal and non-thermal electrons. We also include radiative and collisional recombination, and ionization via photoionization and collisions with both thermal and non-thermal electrons. The resulting matrix equation is numerically solved with the gsl_linalg_LU_solve function of the GNU Scientific Library[3] (Gough [2009](#)).

2.4 Treatment of non-thermal energy deposition

The majority of the emission from SNe Ia is powered by energy injection from nuclear decays (Colgate & McKee [1969](#)). The

---

[3]Available at http://www.gnu.org/software/gsl/

decays of ^{56}Ni, ^{56}Co, and ^{48}V produce γ-rays, which deposit energy into the plasma via Compton scattering with free and bound electrons. A fraction of these decays also produce positrons, which deposit their energy locally (Axelrod [1980](#)) and we assume that the positron deposition takes place within the same grid cell as the decaying nuclei. We also assume that all deposited energy is injected uniformly at a constant rate within each grid cell during each time-step.

We calculate the total (high-energy) deposition rate density in a grid cell by adding the estimated absorption rate of γ-ray packets to the positron contributions from the decays of ^{56}Co and ^{48}V. Using the Bateman equation for the radioactive decay chain ^{56}Ni $\xrightarrow{\tau=8d}$ ^{56}Co $\xrightarrow{\tau=113d}$ ^{56}Fe, the number density of ^{56}Co nuclei is

$$n_{Co56}(t) = \frac{\lambda_{Ni56}}{\lambda_{Co56} - \lambda_{Ni56}} \left(e^{-\lambda_{Co56}t} - e^{-\lambda_{Ni56}t} \right) \frac{\rho(t) X_{0,Ni56}}{M_{Ni56}}, \tag{4}$$

where λ_{Ni56} and λ_{Co56} are inverse mean-lifetimes (τ^{-1}) of ^{56}Ni and ^{56}Co, $\rho(t)$ is the mass density at time t, $X_{0,Ni56}$ is the initial mass fraction of ^{56}Ni in the cell, and M_{Ni56} is the mass of a ^{56}Ni nucleus. The number of ^{56}Co decays per unit time, per unit volume is obtained by multiplying equation (4) by λ_{Co56}. While 81 per cent of ^{56}Co decays proceed via electron capture, the remaining 19 per cent proceed via emission of a positron with an energy in the range 0–1.459 MeV, and a mean energy of 610 keV. Hence, the energy deposited per unit time, per unit volume due to positrons emitted in ^{56}Co decays is given by

$$D_{e^+,Co56} = 0.19 \times 610\,\text{keV} \times \lambda_{Co56} \times n_{Co56}. \tag{5}$$

Similarly for the decay of ^{48}V, which proceeds 49 per cent of the time with the emission of positrons having a mean energy of 290 keV,

$$D_{e^+,V48} = 0.49 \times 290\,\text{keV} \times \lambda_{V48} \times n_{V48}. \tag{6}$$

The total energy deposition rate then is the sum of positron and gamma-ray deposition components,

$$D_{tot} = D_\gamma + D_{e^+,Co56} + D_{e^+,V48}, \tag{7}$$

where D_γ is rate of deposition due to gamma-ray absorption.

At the low densities of SN Ia ejecta several hundred days after explosion, the high-energy electrons and positrons resulting from the energy deposition are not effectively thermalized, leading to a population of high-energy leptons with a non-thermal distribution of energies. As the high-energy particles slow down and secondary electrons are produced by ionizations, the resulting electron energy spectrum contributes a high-energy tail to the Maxwellian distribution of the thermal electrons. These non-thermal particles contribute to the ionization and excitation of ions, and heating of the thermal electrons.

To treat the energy deposition as merely a heating source for the thermal pool of electrons (which is a good approximation at early times) is inadequate for the nebular phase, during which the ionization balance is largely controlled by collisions between ions and non-thermal electrons (Kozma & Fransson [1992](#)). We therefore require a treatment of the ionization and heating caused by non-thermal electrons.

We use a detailed treatment to account for the contributions to heating, excitation, and ionization from non-thermal electrons by first calculating the non-thermal energy distribution using the Spencer–Fano equation (Spencer & Fano [1954](#)) as explained below.

2.5 The non-thermal degradation equation

The Spencer–Fano equation is a specific case of the Boltzmann equation that balances the number of electrons entering and leaving each energy interval. Inside supernova ejecta, the sources and sinks are the energy injected by γ-rays and positrons, excitation, and ionization of ions, and Coulomb scattering with thermal electrons.

The calculated deposition rate from equation (7) is used to scale a source function ($S(E)$, where E is the energy) with a top-hat profile across the narrow range of energies (~ 15.5–16 keV). The particular energy at which we apply the non-thermal deposition does not alter the solution significantly, provided it is high enough for the ionization rates to converge. Our testing found that the ionization rates of Fe ions converged to a tolerance of about 10 per cent by increasing the injection energy above 16 keV.

We numerically solve an integral form of the Spencer–Fano equation similar to Kozma & Fransson (1992) but with an additional term to account for Auger electrons released from ionizations of inner shells,

$$
\sum_j n_j \sum_k \int_E^{E+E_{j\to k}} y(E')\sigma_{\text{exc},j\to k}(E')\mathrm{d}E' + y(E)L_e(E)
$$
$$
+ \sum_i N_i \sum_m \int_E^{E_\text{max}} y(E') \int_{E'-E}^{(E'+E)/2} \sigma_{\text{ion},m}(E',\epsilon)\mathrm{d}\epsilon\,\mathrm{d}E'
$$
$$
= \sum_i N_i \sum_m \int_{2E+I_m}^{E_\text{max}} y(E') \int_{E+I_m}^{(E'+I_m)/2} \sigma_{\text{ion},m}(E',\epsilon)\mathrm{d}\epsilon\,\mathrm{d}E'
$$
$$
+ \sum_i N_i \sum_m \int_E^{E_\text{max}} \delta(E'-\bar{E}_{\text{Auger},m})\mathrm{d}E'
$$
$$
\times \int_E^{E_\text{max}} y(E')\sigma_{\text{ion},m}(E')\mathrm{d}E' + \int_E^{E_\text{max}} S(E')\mathrm{d}E', \tag{8}
$$

where summation runs over ions (i), energy levels (j and k), and electron shells (m), n_j is the population density of level j, $E_{j\to k}$ and $\sigma_{\text{exc},j\to k}$ are the energy difference and cross-section of the excitation transition from level j to k, N_i is the population density of ion i, $\sigma_{\text{ion},m}$, and I_m are the impact ionization cross-section and ionization potential of electron shell m, L_e is the loss function for Coulomb interactions with thermal electrons (which we calculate identically to Kozma & Fransson 1992), and E_max is the maximum energy up to which the solution is defined. The solution to equation (8) is the energy degradation function $y(E) = \mathrm{d}f/\mathrm{d}E$, where f is the electron number flux. Thus, y is a distribution function for the flux of non-thermal particles.

Similar to Li et al. (2012), we use the electron-impact ionization cross-section ($Q_{\text{ion},m}$) fitting formula of Younger (1981), with data from Arnaud & Rothenflug (1985) and Arnaud & Raymond (1992). To obtain the differential cross-sections, we estimate the energy distribution of ejected electrons with the formula of Opal, Peterson & Beaty (1971),

$$
P(E_p, E_s) = \frac{1}{J \arctan[(E_p - I_m)/2J_m]} \frac{1}{1 + (E_s/J_m)^2}, \tag{9}
$$

where I_m is the ionization potential of shell m, E_p, and E_s are the energies of the primary and secondary electrons, and J_m is a fitting parameter that acts as a cut-off energy for secondary electrons. Following Kozma & Fransson (1992), we use $J_m = 24.2$ eV for Ne I, and $J_m = 10.0$ eV for Ar I, as measured by Opal et al. (1971) and $J_m = 0.6I_m$ for all other ions. The differential cross-section is then

$$
\sigma_{\text{ion},m}(E,\epsilon) = Q_{\text{ion},m}(E)P(E,\epsilon - I_i), \tag{10}
$$

where $\sigma_{\text{ion},m}$ is the total cross-section and ϵ is the kinetic energy of the secondary electron.

We have implemented the capability to include excitation of bound electrons by non-thermal collisions for a subset of the permitted lines, making use of the van Regemorter (1962) approximation with a Gaunt factor estimated from the first two terms of the fitting formula given in equation 5 of Mewe (1972). However, this part of the simulation is particularly computationally demanding, and consequently this part of the implementation is not used in the initial simulations presented here.

The solution to equation (8) at energy E only depends on quantities evaluated at energies between E and E_max. This means that when we discretize the integrals, the resulting set of linear equations forms an upper-triangular matrix that is easily solved on a computer. The solution vector then contains the electron degradation spectrum y evaluated on our grid of energy points.

2.6 Non-thermal ionization rates

With a known electron degradation spectrum, the fraction of deposition energy going into ionization of electron shell s of ion i is obtained from

$$
\eta_s = \frac{N_i I_s}{E_\text{init}} \int_{I_s}^{E_\text{max}} \sigma_s(E)y(E)\,\mathrm{d}E, \tag{11}
$$

where I_s and σ_s are the ionization potential and impact ionization cross-sections of shell s. Similarly, the non-thermal ionization rate of ion i is given by

$$
\Gamma_i N_i = \frac{N_i \epsilon_\text{dep}}{E_\text{init}} \sum_s \int_{I_s}^{E_\text{max}} \sigma_s(E)y(E)\,\mathrm{d}E. \tag{12}
$$

When a non-thermal electron impact frees an electron from an inner shell, the relaxation of the resulting ion can eject further bound electrons (the Auger effect). In our standard ARTIS models, we use the probabilities of ejecting one or two Auger electrons given by Kaastra & Mewe (1993) to calculate rates of double and triple ionization in the non-LTE population/ionization solver.[4] Note, however, that we do not currently follow the photons produced in the refilling of inner shells, but we do include an extra term in our form of the Spencer–Fano equation to allow Auger electrons to contribute to heating, ionization, and excitation.

3 VERIFICATION OF METHOD

In this section, we present the results of several calculations made to test and demonstrate the newly implemented code features. We first show the results of an idealized test of the non-thermal solver (Section 3.1) in which only a single element is included. We then (Section 3.2) present and discuss a full-spectrum synthesis calculation for the well-known W7 model (Nomoto et al. 1984; Iwamoto et al. 1999).

3.1 Non-thermal solver

To verify our implementation of the Spencer–Fano solver, we calculate the electron degradation function for a pure-O plasma with

---

[4]That is, in the solver, the ionization rate is used to connect the target ion to the ground states of the species with one degree higher ionization (rate proportional to probability of no Auger electron), two degrees higher (proportional to rate for one Auger electron, etc.).
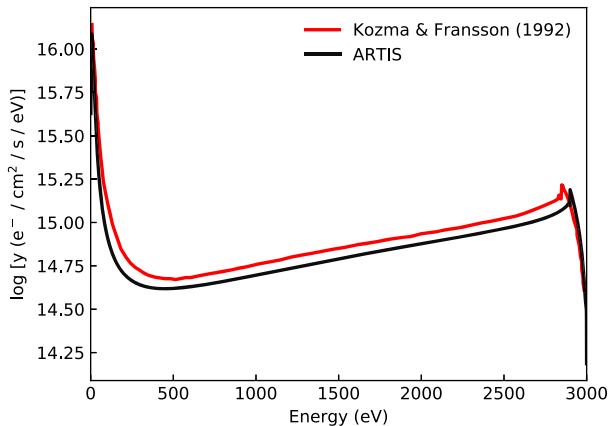
Figure 1. Electron degradation function, y for a pure-O plasma using ARTIS (black). With the same thermal electron density (10^8 cm^{-3}) and ionization fraction (10^{-2}), and a similar source function (spread across 2.9–3.0 keV), the ARTIS result is similar to Kozma & Fransson (1992). The red line has been digitized from fig. 1 of Kozma & Fransson (1992).

the same ionization fraction (0.01) and free electron density (10^8 cm^{-3}) as Kozma & Fransson (1992). The degradation function is shown in Fig. 1, with a digitized version of the degradation function in fig. 1 of Kozma & Fransson (1992) for comparison. We find close agreement, with a small difference that is likely due to differences in the chosen source function, i.e. the distribution of energies at which we inject the non-thermal energy.

3.2 W7 calculation

To more fully test the nebular-phase capabilities of the code, we have carried out test calculations for the nebular spectrum at 330 (post-explosion) for the W7 model of Nomoto et al. (1984) with the nucleosynthesis of Iwamoto et al. (1999). The W7 model is derived from a 1D simulation of the deflagration of a $M_{\rm ch}$ C-O WD with the deflagration speed having been chosen to yield an overall good level of agreement with the known properties of normal SNe Ia. We adopt this model for our tests since it is well known in the literature and has been widely used in previous studies (Ruiz-Lapuente et al. 1995; Liu et al. 1997; Sollerman et al. 2004). In particular, adopting this model (and epoch) allows us to directly compare with the existing nebular-phase spectrum synthesis calculations made with the SUMO code (see Section 3.2.4). It should be noted, however, that this version of the W7 model is not fully representative of modern Chandrasekhar mass models. For example, revisions to the nucleosynthesis yield calculations (Leung & Nomoto 2018; Nomoto & Leung 2018) involve significant updates for some of the isotopes relevant to the nebular phase. More importantly, the 1D symmetry of the model is not well justified based on modern multidimensional explosion simulations (e.g. Seitenzahl et al. 2013; Sim et al. 2013). We will address these questions in subsequent studies in which modern multidimensional explosion simulations will be used.

3.2.1 Ionization and thermal structure

The structure of the inner ejecta is of primary relevance to understanding late-phase supernova spectra (the outer ejecta having expanded sufficiently to be optically thin in most places). The inner part of the W7 model includes a core of stable Ni isotopes and

Fe (produced by electron capture during the explosion), which is surrounded by a ^{56}Ni-rich region. This composition profile is shown in the top panel of Fig. 2.

In our calculation (epoch of 330 d post-explosion), we find that the core of stable material is at low temperature ($\sim$3000 K) and is mostly singly ionized (temperature and ionization fractions are shown in Fig. 2). The temperature and ionization then rise rapidly through the (initially) ^{56}Ni-rich region leading to a peak of $\sim$9000 K and predominantly two to three times ionized material in the ejecta around $\sim$8000 km s^{-1}. This thermal/ionization structure is in generally good (albeit imperfect) agreement to that calculated for the W7 model by Liu et al. (1997) (see their fig. 1, which shows ejecta properties for an epoch of 300 d). One difference is that our Fe$^+$ abundance fraction becomes very low (below 10^{-2}) in the ^{56}Ni-rich region between 6000 to 9000 km s^{-1}, due to the high photoionization rate in these zones.

3.2.2 Non-LTE populations

A key improvement in the new version of ARTIS used here is the implementation of our NLTE population solver. As one example of the importance of the strength of non-LTE effects, Fig. 3 shows the calculated departure coefficients of the first 17 levels of Ni II in one of the ^{58}Ni-rich model cells (selected at 4000 km s^{-1}) of our W7 calculation (at 330 d post-explosion). This demonstrates that the populations of excited states that are responsible for observable emission features in SNe Ia spectra can be expected to depart significantly from LTE (Axelrod 1980).

As a test of our NLTE populations, we compared our departure coefficients to those calculated with a collisional-radiative model, which assumes statistical equilibrium between thermal electron collisions and radiative decays. Specifically, we utilized the CHIANTI atomic data base and analysis package (Dere et al. 1997; Del Zanna et al. 2015) to compute departure coefficients adopting the electron temperature and free electron density obtained from ARTIS. Although this is a substantial simplification compared to the full treatment in the code, the relatively high electron temperature ($T_e = 7940.1$ K) and low radiation field intensity obtained in this region of the model at this time means that the populations of the first few levels are primarily controlled by thermal electron collisions and spontaneous radiative decay. The CHIANTI model includes only 17 levels, which causes the departure coefficients to diverge from our model from around level 9 and above. These levels are significantly populated by radiative decays from higher levels that are not included in CHIANTI. As shown in Fig. 3, the level of agreement is generally good (typically a few tens per cent, or better).

3.2.3 Radiation field consistency check

Fig. 4 shows the internal radiation field reconstructed from our Monte Carlo estimators (see Section 2.2) for an (initially) ^{56}Ni-rich zone at 7000 km s^{-1} in the W7 model at 330 d. For comparison, Fig. 4 also shows a single dilute blackbody model for the full spectrum and the external radiation field (i.e. emergent simulation spectrum) scaled to the radius of the cell. The internal radiation field has a similar spectral energy distribution to the emergent radiation field (aside from a Doppler shift, see Fig. 5), as would be expected for the approximately optically thin conditions of the nebular phase. Clearly, the radiation field model represents an improvement compared to the full-spectrum dilute blackbody model in previous ARTIS simulations.
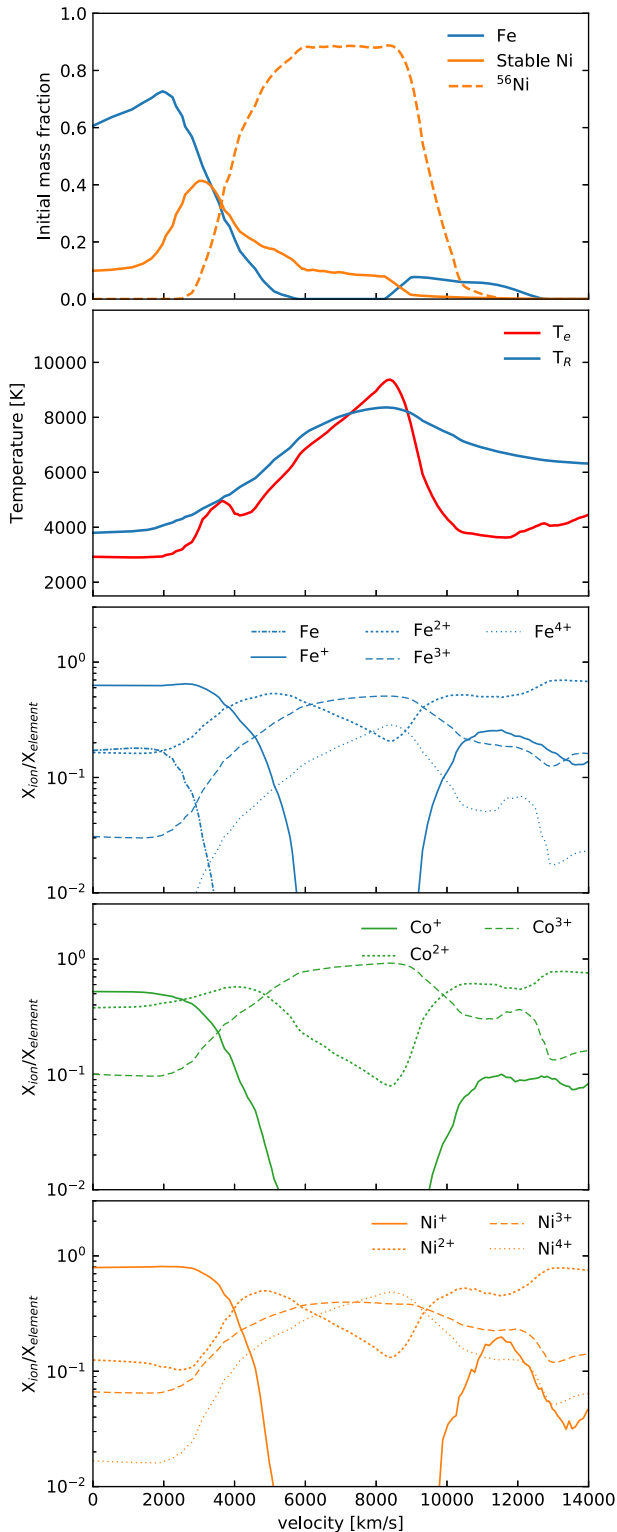
Figure 2. Composition immediately after explosion (top panel), and at 330 d: the electron temperature (T_e) and radiation temperature (T_R) (second panel), Fe ion balance (third panel), Co ion balance (fourth panel), and Ni ion balance (bottom panel) as a function of velocity for the inner ejecta of the ARTIS W7 model. By this time, most of the initial ^{56}Ni will have decayed into ^{56}Co and ^{56}Fe.

3.2.4 W7 nebular spectrum comparison

In Fig. 6 (to be compared with Figs 7 and 8 in Section 4.3), we show the computed spectrum in the optical and near-infrared (near-IR) regions for our ARTIS W7 calculation at 330 d with colour coding to illustrate the ions responsible for the emission. Specifically, each of our Monte Carlo quanta is tagged by their last interaction with the thermal pool (i.e. their last *k*-packet interaction in the nomenclature of Lucy 2002). This gives an indication of the contributions of the different ions to the cooling of the ejecta. Note, however, that some packets do undergo fluorescence/scattering by other ions prior to escape from the simulation, which is not captured by this simple tagging scheme.

In agreement with previous studies of nebular spectra for SNe Ia (Axelrod 1980; Ruiz-Lapuente & Lucy 1992; Liu et al. 1997) the strongest peak of the spectrum is formed mostly by [Fe III] $\lambda\lambda$4658, 4701 emission, with contributions from other transitions between the states in the low-lying ^{3}F2 term and ^{5}D ground term. Much of the rest of the spectrum in the optical is due to [Ni II] and [Ni III], and the near-IR is dominated by [Fe II], with several strong contributions from [Ni II]. Strong features of [Ni II] in particular are the $\lambda\lambda$7378, 7412 doublet ($3p^63d^8(^3F)4s\ ^2F_{7/2} \rightarrow 3p^63d^9\ ^2D_{5/2}$ and $3p^63d^8(^3F)4s\ ^2F_{5/2} \rightarrow 3p^63d^9\ ^2D_{3/2}$) in the optical and [Ni II] ($3d^8(^3F)4s\ ^2F_{7/2} \rightarrow 3d^8(^3F)4s\ ^4F_{9/2}$) at 1.939 μm in the near-IR. As has been previously noted, the W7 model predicts relatively strong [Ni II] compared to observations (see e.g. Liu et al. 1997), and we also find similarly strong features to Liu et al. (1997), Ruiz-Lapuente et al. (1995), Sollerman et al. (2004), Maeda et al. (2010), Maurer et al. (2011), Mazzali et al. (2011), and Fransson & Jerkstrand (2015).

The lateness of the epoch considered here means that Co emission is comparatively weak, and we do not find significant influence from other elements across most of the spectral region considered: the most notable contribution is from S III between 9000 and 10 000 Å. This feature is due to emission from the [S III] $\lambda\lambda$9069, 9530 lines ($3s^23p^2\ ^1D_2 \rightarrow\ ^3P_{1,2}$).

In Fig. 5, we compare our optical spectrum for the W7 model at 330 d after explosion with the spectrum of Fransson & Jerkstrand (2015),[5] which has been calculated using the SUMO radiative transfer code described by Jerkstrand, Fransson & Kozma (2011) with updates described by Jerkstrand et al. (2015). We note that the SUMO spectrum of W7 at 330 d is generally similar to the spectra produced by the Mazzali et al. (2001) and NERO codes (figs 5 and 6 of Maurer et al. 2011). In general, the spectra from the ARTIS and SUMO calculations are extremely similar. However, there are several minor quantitative differences which may be related to differences in approach.

The SUMO calculation includes neutral species and ions up to doubly ionized for Fe, Co, and Ni, but does not consider higher ions (i.e. Fe^{3+} and above). In contrast, our calculation neglects neutral Co and Ni but includes the triply ionized species for all three of these elements. SUMO includes several hundred non-LTE levels for Fe-group elements, while we use 80 for most ions, and 197 for Fe^+. Another difference is that the SUMO calculation substitutes the valence-shell potential for the inner-shell potential when calculating the ionization rates (equation 12) as a way of compensating for multiple ionizations resulting from Auger electrons. In ARTIS, we use the individual shell potentials and their Auger yields (see

---

[5]Available at https://star.pst.qub.ac.uk/webdav/public/ajerkstrand/Models/
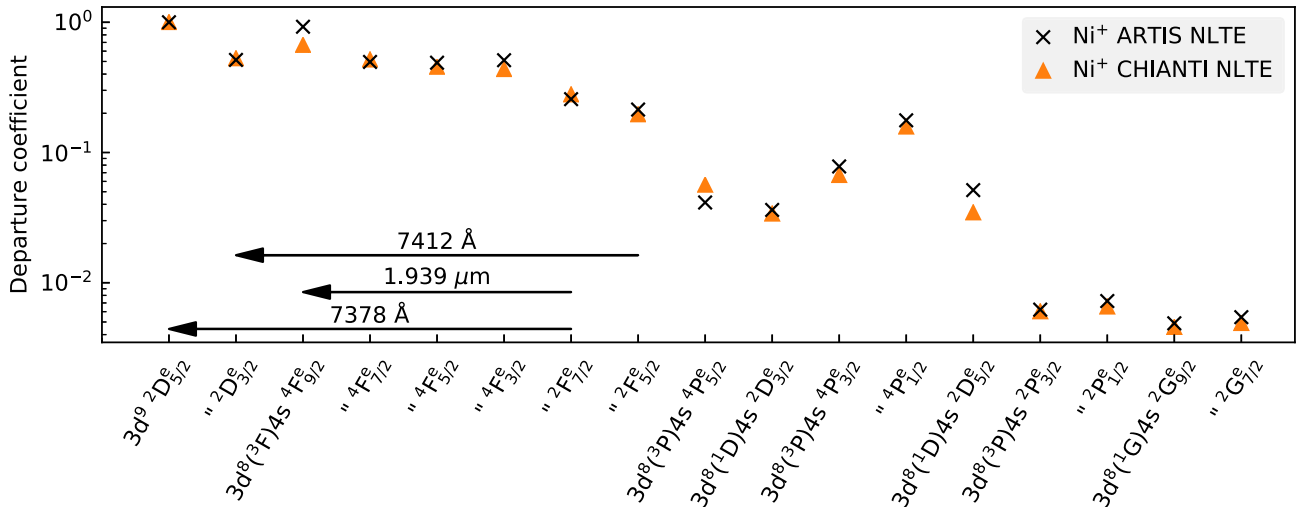FranssonJerkstrand2015/W7_330d.dat

Figure 3. Non-LTE departure coefficients (population relative to the ground state, divided by the same quantity for Boltzmann equilibrium at the electron temperature) for Ni II in a ^{56}Ni-rich region near 4000 km s^{-1} in the W7 model at 330 d. Also shown is reference data from CHIANTI in a collisional-radiative model at the same electron temperature (7940.1 K) and electron density (1.1×10^6 cm^{-3}). The arrows represent several important transitions that are the most likely to produce observable spectral features – the $\lambda\lambda 7378, 7412$ doublet and the 1.939 μm near-IR line.
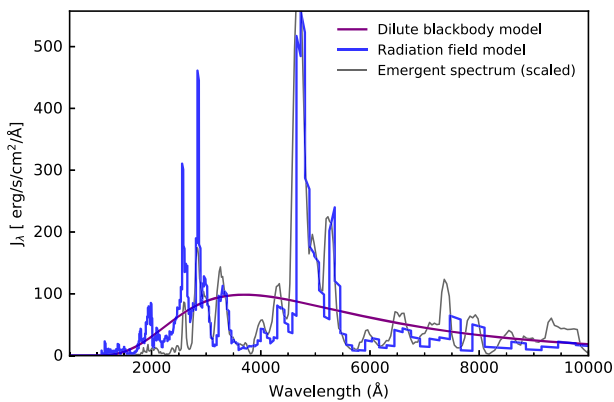
Figure 4. Radiation field estimators compared with the emergent spectrum for an (initially) ^{56}Ni-rich cell near 7000 km s^{-1} in the W7 model at 330 d. This figure shows the full-spectrum fit dilute blackbody field (purple) and the binned dilute blackbody fits (blue) that describe the radiation field for ARTIS in this work. Because this cell has a relatively high radiation temperature, the radiation field is typically greater at bluer wavelengths compared to the outgoing spectrum.
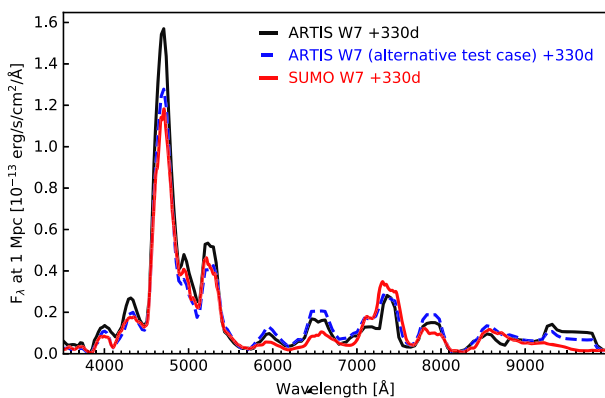
Figure 5. Nebular spectra of the W7 model at 330 d calculated with ARTIS (black) and with SUMO (red). We also show (in blue) the spectrum from a test ARTIS calculation (see the text).

Section 2.6) to determine the rates of single, double, and triple ionization. It may therefore be expected that our approach may provide more accurate ionization rates, while the SUMO treatment may give an upper bound on the total ionization rates. However, our testing found that the consequences of these multiple ionizations for the resulting spectra are a minor effect.

To explore some of these issues, we have carried out a second ARTIS test calculation (blue dashed line in Fig. 5) in which we (i) do not include Fe^{3+}, Co^{3+} or Ni^{3+} (or higher ions), (ii) divide ionization energies by the valence potentials and set the Auger probabilities to zero, and (iii) use the Shull & van Steenberg (1982) recombination rate for Ni^{2+}. This test calculation fits the [Fe II] and [Fe III] features of SUMO very precisely. However, the [Ni III] features (which were already stronger than SUMO in our reference calculation) become even stronger, which is probably mostly due to the slower recombination rate of Ni^{2+} to Ni$^+$.

The SUMO calculation does not include [S III] emission lines and thus does not match ARTIS in the region around $\sim$ 9000–10 000 Å. We note, however, that a similar feature is found in the nebular spectra calculated by Wilk, Hillier & Dessart (2018).

4 SUB-CHANDRASEKHAR DETONATION MODELS

As a first application of the code developments described above, we present nebular-phase spectra for sub-$M_{\rm ch}$ detonation models.

4.1 Motivation

The relatively low densities in sub-$M_{\rm ch}$ explosion models makes electron capture inefficient when compared to $M_{\rm ch}$ explosion scenarios. Consequently the yields of neutron-rich isotopes, such as ^{54}Fe and ^{58}Ni, are relatively small compared to Chandrasekhar mass deflagration models. This is one promising way to distinguish Chandrasekhar mass and sub-$M_{\rm ch}$ explosion models. In particular, ^{58}Ni is of special interest since its presence is directly probed by nebular-phase spectra (although ^{58}Ni is a minor contribution to the
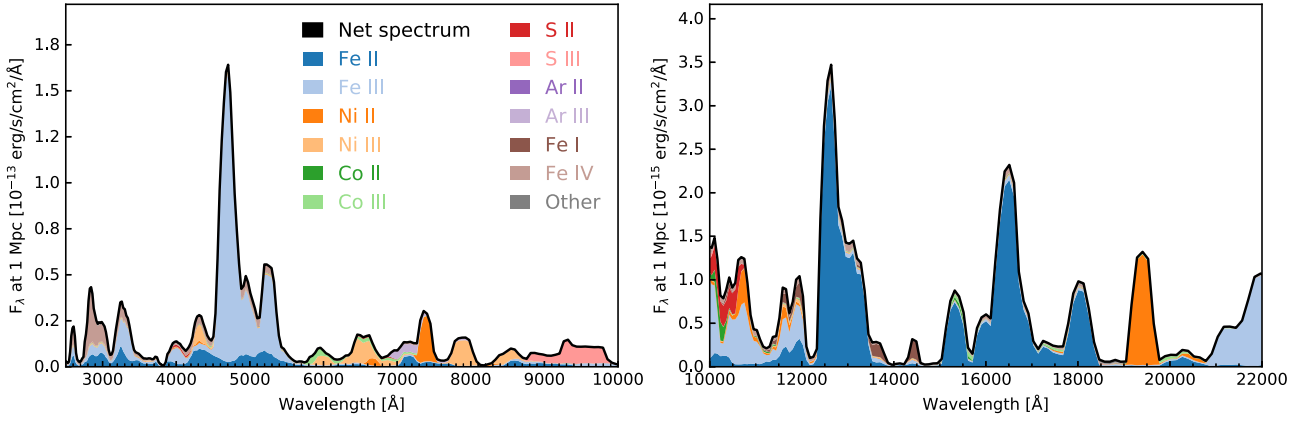
Figure 6. Nebular emission spectra of the W7 model at 330 d in the optical (left) and near-infrared (right). The total spectrum is plotted as the black curve. The area under the spectrum is colour coded to indicate which ions are responsible for the emission in each wavelength bin (see the text). Note the differing scales on left-hand and right-hand panels.
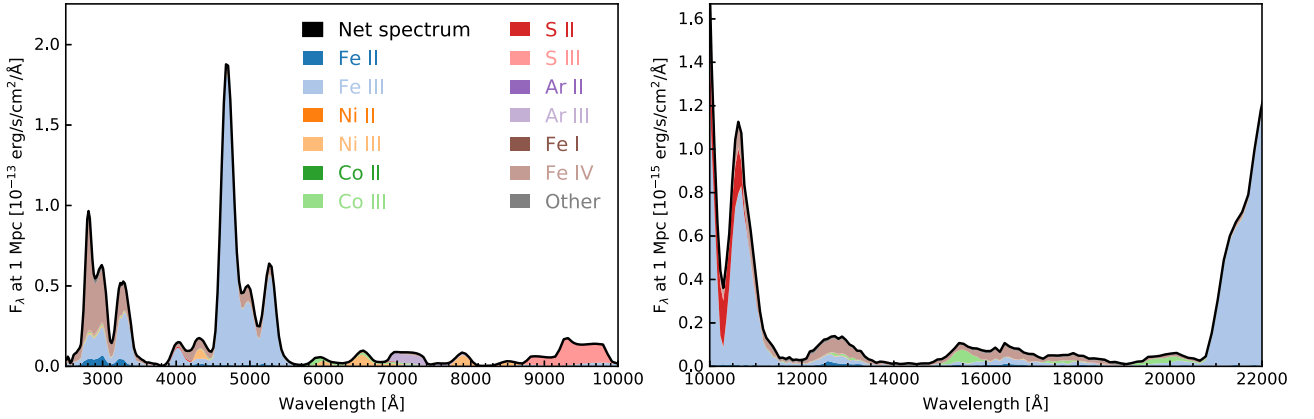

Figure 7. Nebular spectra coloured by ion for S0 ARTIS models at 330 d in the optical (left-hand panel) and near-infrared (right-hand panel). Note the differing scales on left-hand and right-hand panels.
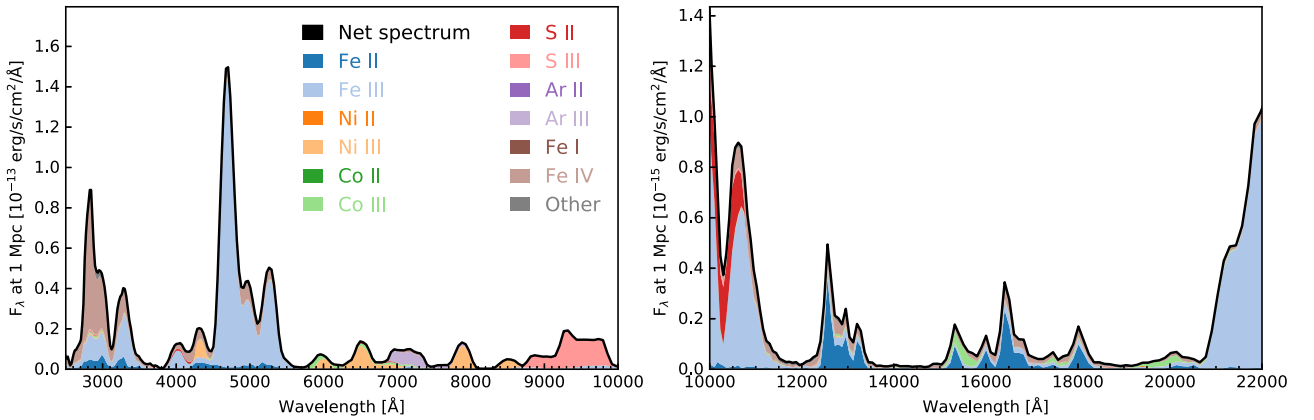
Figure 8. Nebular spectra coloured by ion for S5.5 ARTIS models at 330 d in the optical (left-hand panel) and near-infrared (right-hand panel). Note the differing scales on left-hand and right-hand panels.

overall Ni abundance immediately post-explosion, the relatively rapid decay of ^{56}Ni means that ^{58}Ni becomes dominant at late times).

However, sub-M_{ch} models do produce some stable Fe-group material owing to the presence of the neutron-rich nuclide ^{22}Ne in the progenitor. This isotope increases the neutron-to-proton ratio in the fuel, which when burned to nuclear statistical equilibrium, results in an enhanced production of stable Fe-group nuclides (e.g. Timmes, Brown & Truran 2003; Seitenzahl & Townsley 2017). Understanding the influence of ^{22}Ne in sub-M_{ch} models is potentially complicated by the action of gravitational settling in WD stars. This process can cause the neutron-rich ^{22}Ne nuclei to accumulate near the centre (Deloye & Bildsten 2002; García-Berro, Althaus & Córsico 2008). As a consequence, the explosion of a gravitationally settled WD model may produce more stable Fe-group material near the centre. This is somewhat reminiscent of scenarios in which the inner ejecta have a high concentration of stable Fe-group elements as found in 1D delayed-detonation models (and has been inferred from observations, e.g. Mazzali et al. 2007). However, the effect is different in origin and much less pronounced (i.e. although ^{22}Ne settling may lead to an enhanced abundance of stable material in the inner ejecta, it is not expected that it will produce a core dominated by stable isotopes; see also Bravo et al. 2011). Here, our objective is to quantify this issue by calculating nebular-phase spectra for simple detonation models of sub-M_{ch} WDs in which the progenitor WD contains different radial profiles of ^{22}Ne.

4.2 Adopted models

We study two specific sub-M_{ch} detonation models. They were calculated by Michel (2014) using the hydrodynamics code LEAFS (Reinecke, Hillebrandt & Niemeyer 2002; Röpke 2005) following the same approach described by Sim et al. (2010) and Marquardt et al. (2015).

In both cases, the initial WD is hydrostatic and has a total mass of $1.06\,M_\odot$. The models differ, however, in the adopted composition structure of the WD: specifically in the distribution of ^{22}Ne. In the first model (hereafter 'S0' model), a uniform mass fraction of $X(^{22}\mathrm{Ne}) = 0.02$ (corresponding to approximately solar metallicity) is adopted throughout the WD: i.e. this represents the limit of no settling.

In the second model, 'S5.5', a $X(^{22}\mathrm{Ne})$ profile was constructed to approximately correspond to an extremely high degree of ^{22}Ne settling. In particular, this is based on the most extreme settling calculated for a $1.06\,M_\odot$ WD in the study by García-Berro et al. (2008) (settling time of 5.544 Gyr and a boosted diffusion coefficient $D = 5D_S$ where D_S is the diffusion coefficient due to gravitational settling; see equation 18 of García-Berro et al. 2008 for details). For the specific simulation carried out here, $X(^{22}\mathrm{Ne})$ has a maximum value of 0.095 at the centre of the WD and decreases monotonically outwards to $X(^{22}\mathrm{Ne}) = 0$ at mass coordinate $M = 0.4\,M_\odot$ (for simplicity, a sine-squared functional form was adopted, see Fig. 9). In both models, it was assumed that the WD initially consists of C and O in equal parts. We further assume that C and O are substituted in equal parts during the settling of ^{22}Ne. This is a simplification since the settling depends on the proton number Z and the nucleon number A of the surrounding material and also differs from García-Berro et al. (2008), who studied the ^{22}Ne settling in a pure C environment for simplicity.

The hydrodynamical explosion simulations were performed in the manner described by Marquardt et al. (2015), including calibration of detonation energy-release tables for the appropriate

Table 1. Synthesized masses of ^{56}Ni, ^{54}Fe, and ^{58}Ni from the W7, S0, and S5.5 explosion models.

Model	Synthesized mass		
	^{56}Ni ($M_\odot$)	^{54}Fe ($10^{-2}\,M_\odot$)	^{58}Ni ($10^{-2}\,M_\odot$)
W7[a]	0.59	9.5	11.0
S0	0.56	2.0	1.8
S5.5	0.55	1.2	3.4

[a]The W7 nucleosynthesis used here is that of Iwamoto et al. (1999). We note that significantly lower yields of ^{58}Ni have been found in the updated calculations described by Nomoto & Leung (2018).

compositions. Sets of nucleosynthesis tracer particles were then processed using the 384-isotope network of Travaglio et al. (2004), from which the ejecta profiles were derived for the homologous expansion phase (see Marquardt et al. 2015 for a description of the methods).

As expected from the discussion above, the most important difference in structure between the two explosion models is in the distribution of Fe-group elements. In particular, the ^{56}Ni mass fraction in the S0 model is almost uniform throughout the inner ~8000 km s^{-1} of the model (accompanied by an approximately uniform composition of stable Fe and Ni). In contrast, ^{22}Ne settling in the S5.5 model leads to an enhanced concentration of stable Ni in the inner core with a maximum in the ^{56}Ni distribution around 8000 km s^{-1} (see Fig. 10). This central concentration of stable isotopes is qualitatively reminiscent of the W7 model (see Fig. 2) although *much* less pronounced. The enhanced production of ^{56}Ni at the expense of stable Fe outside 8000 km s^{-1} in the S5.5 model is due to the lack of ^{22}Ne in the outer layers.

Table 1 shows the synthesized masses of ^{56}Ni, ^{54}Fe, and ^{58}Ni from the W7, S0, and S5.5 explosion models. Compared to the S0 model, the S5.5 model has synthesized a few per cent less ^{56}Ni, 40 per cent less ^{54}Fe, and of particular importance for the nebular spectra, 85 per cent more ^{58}Ni mass.

4.3 Overview of calculations

We have calculated ARTIS nebular spectra for both S0 and S5.5 for a range of epochs between 220 and 360 d for both models. Fig. 10 shows the temperatures and ionization balance for both models at 330 d (i.e. the same epoch for comparison to W7 as shown in Fig. 2). Compared to W7, the S0 and S5.5 models exhibit significantly higher ionization, particularly in the core region, but also generally throughout the ejecta (compare bottom panels of Figs 2 and 10). Compared to the S0 model, the core of stable IGEs in the S5.5 model leads to lower electron temperatures and a lower ionization state among Fe-group species at 330 d. However, the S5.5 model is still hotter and more highly ionized than W7 throughout the core of the ejecta.

Figs 7 and 8 show the spectra of the ARTIS models for S0 and S5.5 at 330 d coloured by the emitting ion. Despite the differences in composition and temperatures, both models show broadly similar spectra to each other: dominated by emission of Fe-peak elements. However, there are clear differences that allow the models to be distinguished from W7. In the optical, the most noticeable difference between W7 and the detonation models is in the emission of Ni II. Both of the sub-M_{ch} models predict negligible emission by [Ni II] $\lambda\lambda$7378, 7412 and the difference between the settling (S5.5) and the homogeneous (S0) model is not visible in this feature. Due to the high ionization state, the additional Ni abundance from increased
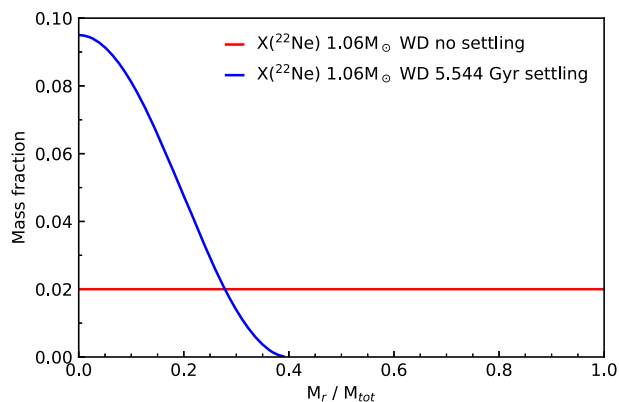
Figure 9. ^{22}Ne profiles adopted for the WD pre-explosion models with no settling (S0, red) and after 5.544 Gyr of boosted gravitational settling (S5.5, blue).

stable ^{58}Ni in S5.5 results in stronger [Ni III] features than the S0 model. In addition, the [Fe II] features are much stronger in our W7 calculation than in the detonation models (a consequence of the lower ionization state) and we note that absorption by Fe I is much less important in the detonation models than in W7 (see Section 3.2.4).

In the near-IR, only the W7 ARTIS calculations produce a clear [Ni II] 1.939 μm emission feature. This feature has been discussed in the context of synthetic spectra for models with stable Ni by Blondin, Dessart & Hillier (2018) and Wilk et al. (2018), and is a particularly useful signature of Ni since it is relatively unblended (Dhawan et al. 2018; Flörs et al. 2020) (see right-hand panels of Figs 7 and 8). Near-IR emission features from [Fe II] are virtually absent in the S0 model, while in S5.5 they become significant and exhibit a similar distribution to W7 (although they are much weaker than for W7).

4.4 Comparison to observations

Figs 11 and 12 show our synthetic spectra for the W7 and two sub-$M_{\rm ch}$ models compared to observed spectra at two epochs (220 and 360 d after explosion) for wavelengths from the optical to the near-IR. The objects selected for comparison (SN2013ct and SN2013aa) have been chosen from the observed sample of Maguire et al. (2016) for their simultaneous coverage in optical and near-IR at epochs roughly matching those of our ARTIS simulations. Both objects are spectroscopically normal SNe Ia (Maguire et al. 2013, 2016), and the observed spectra have been corrected for redshift, reddening, and distance using the same values as Maguire et al. (2016). Since the observed SN2013ct spectrum has an uncertain flux calibration, this spectrum has also been scaled by a constant normalization factor for ease of comparison between features and the models. The SN2013aa spectra are shown on the (calibrated) absolute flux scale.

In the optical region of the spectrum at 220 d (top left of Fig. 11), the theoretical models produce a similar complex of [Fe II] and [Fe III] features around 4000–5300 Å. In general the match of these features with the observation shown is reasonable, but there are clear discrepancies. For example around 4300 Å where all of the models fail to reproduce the strength of the clear emission peak as seen in the data. We note that this region was also where some discrepancies between SUMO and ARTIS manifest (see Section 3.2.4), possibly suggesting systematic shortcomings in the modelling. In

agreement with Liu et al. (1997) our W7 model calculation produces an optical [Ni II] λλ7378, 7412 emission that is significantly too strong to match the observed spectrum. The sub-$M_{\rm ch}$ detonation models on the other hand, predict negligible emission from [Ni II]. We note that all our models fail to reproduce the [Fe II] peak around 7200 Å at this epoch. At the later epoch considered (+360 d), the agreement between the models and the observation of SN2013aa is of comparable quality to that between the model and SN2013ct around +220 d. Again, the sub-$M_{\rm ch}$ models produce no significant [Ni II] feature and there are significant discrepancies around [Fe II] 4300 Å, and the main [Fe III] peak is somewhat overproduced.

The right-hand panels of Fig. 11 compare the near-IR spectra of the models to observations (same comparison supernovae and with consistent flux scaling relative to the optical). Here, we note that the [Fe II] emission from the sub-$M_{\rm ch}$ models is substantially too weak compared to the observed spectrum for the 220d SN2013ct spectrum. In contrast, the W7 [Fe II] emission is also too weak but matches this spectrum better, except that the [Ni II] feature at 1.939 μm is far too strong in this calculation.

The weakness of [Fe II] near-IR emission in the sub-$M_{\rm ch}$ detonations can most likely be attributed to the degree of ionization being too high in the calculations. Despite the key role played by non-thermal ionization in the overall ionization structure, we find that photoionization of the singly ionized species is very important throughout much of ejecta – indeed for Fe$^+$ we find that the photoionization rate is comparable to or exceeds the non-thermal ionization rate throughout the ejecta in the sub-$M_{\rm ch}$ models.

The origin of these high photoionization rates is ultimately the photons (bound–free and free–free) produced by the high-ionization species, particularly Fe^{3+} and Fe^{4+}. As first considered by Axelrod (1980) for the case of SNe Ia in their nebular phase, recombination photons emitted by high Fe-group ions can easily photoionize lower ions (and neutral species). The precise amount of 'recycling' of recombination photons is extremely sensitive to the atomic data, ejecta structure, and non-thermal ionization rates but plays an important role in our simulations.

The overionization of sub-$M_{\rm ch}$ models was already found by Ruiz-Lapuente (1996) and is supported by other more recent studies. In particular, our findings are similar to Mazzali et al. (2015) and Wilk et al. (2018): both those studies found that overionization is a challenge for modelling nebular spectra for several different scenarios, particularly sub-$M_{\rm ch}$ models. Possible solutions to overionization proposed include invoking a relatively large mass of stable Fe in the context of Chandrasekhar mass models (i.e. ^{54}Fe, see Mazzali et al. 2015) and/or potential clumping/inhomogeneities in the ejecta (Wilk et al. 2018; Wilk, Hillier & Dessart 2019). We note, however, that at the later epoch we consider the level of discrepancy between the sub-$M_{\rm ch}$ models and the observation of SN2013aa is smaller, albeit acting in the same sense. Also the ratios of the spectral features are predicted to change as the ejecta conditions evolve. This leads to complex changes in the predicted [Fe II] emission but also affects the [Ni II] 1.939 μm feature, which becomes much weaker at 360 d, relative to the other near-IR emission features, in the W7 model.

In summary, our results confirm that photoionization is an important process, even at nebular phases. This highlights the need for ongoing efforts to improve and expand atomic data for the iron-peak elements.

5 SUMMARY

We have extended the validity of our three-dimensional Monte Carlo radiative transfer code ARTIS for SNe Ia up to hundreds of
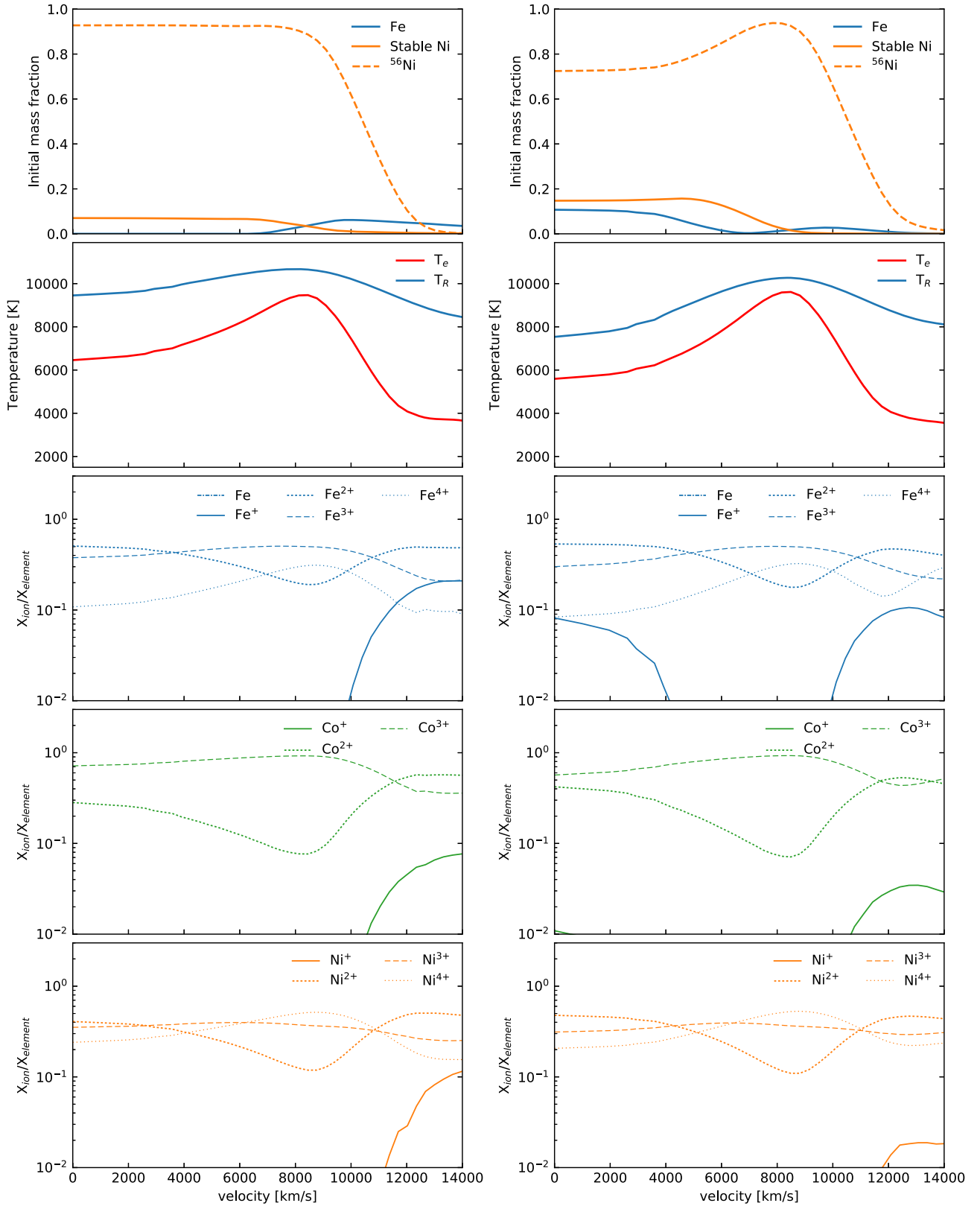
Figure 10. Similar to Fig. 2 but for the sub-$M_{\rm ch}$ detonation models at 330d: S0 (left) and S5.5 (right).
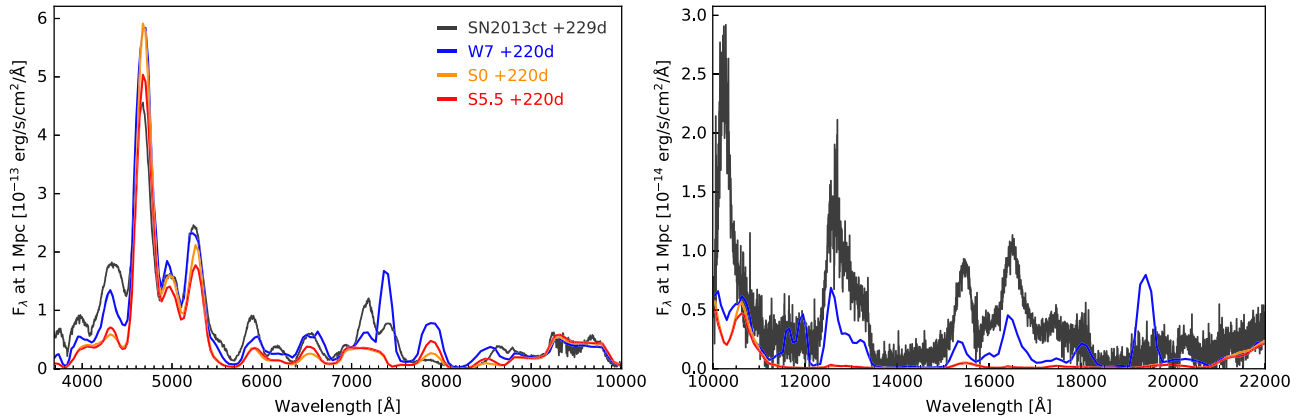
Figure 11. Nebular spectra of W7 and sub-$M_{\rm ch}$ ARTIS models compared to observed spectra of SN2013ct at 229d (Maguire et al. 2016). ARTIS models at 220d in the optical (left) and the near-infrared (right). Note the differing scales on left-hand and right-hand panels.
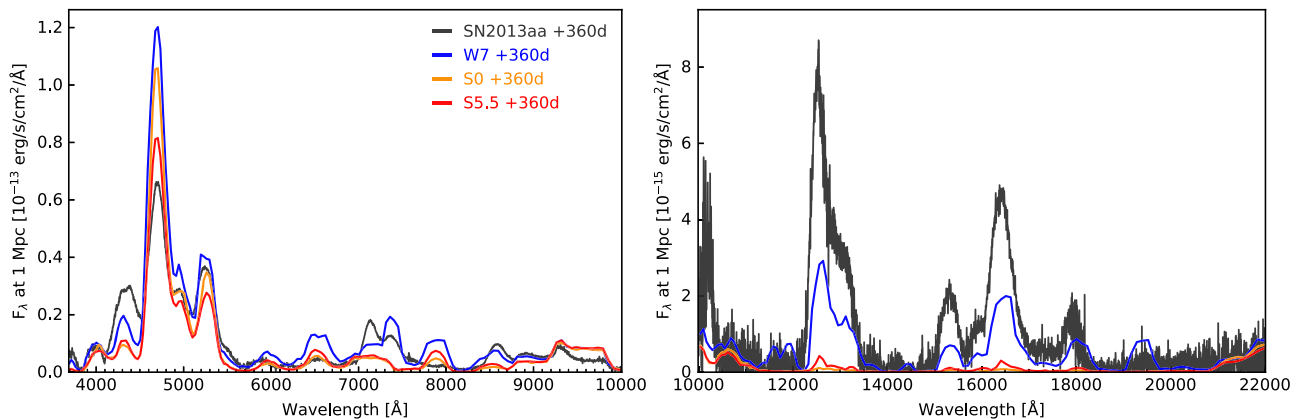

Figure 12. Nebular spectra of W7 and sub-$M_{\rm ch}$ ARTIS models compared to observations of SN2013aa at 360d (Maguire et al. 2016). ARTIS models at 360d in the optical (left) and the near-infrared. Note the differing scales on left-hand and right-hand panels.

days after maximum light. We have achieved this by modelling the relevant physics in the nebular phase, including a detailed treatment of non-thermal electrons (the dominant source of ionization in this phase), a new atomic data set with forbidden transitions, a non-LTE population and ionization solver, and a detailed non-LTE radiation field model. As a test case, we have compared our results for the well-known W7 model with those of SUMO and found generally good agreement, with some discrepancies attributed to differences in the atomic processes.

We investigated the influence of gravitational settling in the nebular-phase spectra of a sub-$M_{\rm ch}$ detonation model, and found that ^{22}Ne settling is relevant to quantitative analysis and interpretation of SNe Ia spectra in the context of sub-$M_{\rm ch}$ models. In particular, settling enhances the predicted [Ni III] features and slightly lowers the ionization balance overall. In agreement with previous studies (Mazzali et al. 2015; Wilk et al. 2018), we do find that overionization is a major issue for sub-$M_{\rm ch}$ models, and represents a considerably larger obstacle for reconciling this scenario with observations than any under- or overprediction of the ^{58}Ni abundance. However, our comparisons for the two epochs considered here suggest that the magnitude of this discrepancy varies, indicating the potential value for future studies in which time series of nebular-phase spectra can be consistently modelled.

In future studies, we intend to apply our radiative transfer method to three-dimensional explosion models, such as the DDT models

of Seitenzahl et al. (2013). These theoretical nebular spectra will help to resolve the degeneracy between candidate SNe Ia scenarios and allow us to more fully quantify the observable signatures of the 3D structure of nucleosynthesis ash as predicted by modern hydrodynamical simulations.

through computational resources at Forschungszentrum Jülich via project HMU14.

REFERENCES

Anderson L. S., 1989, ApJ, 339, 558
Arnaud M., Raymond J., 1992, ApJ, 398, 394
Arnaud M., Rothenflug R., 1985, A&AS, 60, 425
Arnett W. D., 1969, Ap&SS, 5, 180
Arnett W. D., 1979, ApJ, 230, L37
Axelrod T. S., 1980, PhD thesis, California Univ.
Blondin S., Dessart L., Hillier D. J., 2018, MNRAS, 474, 3931
Bloom J. S. et al., 2012, ApJ, 744, L17
Botyánszki J., Kasen D., 2017, ApJ, 845, 176
Botyánszki J., Kasen D., Plewa T., 2018, ApJ, 852, L6
Bravo E., Althaus L. G., García-Berro E., Dominguez I., 2011, A&A, 526, A26
Bulla M., Sim S. A., Kromer M., 2015, MNRAS, 450, 967
Colgate S. A., McKee C., 1969, ApJ, 157, 623
Deloye C. J., Bildsten L., 2002, ApJ, 580, 1077
Del Zanna G., Dere K. P., Young P. R., Landi E., Mason H. E., 2015, A&A, 582, A56
Dere K. P., Landi E., Mason H. E., Monsignori Fossi B. C., Young P. R., 1997, A&AS, 125, 149
Dhawan S., Flörs A., Leibundgut B., Maguire K., Kerzendorf W., Taubenberger S., Van Kerkwijk M. H., Spyromilio J., 2018, A&A, 619, A102
Dong S., Katz B., Kushnir D., Prieto J. L., 2015, MNRAS, 454, L61
Fink M. et al., 2014, MNRAS, 438, 1762
Flörs A. et al., 2020, MNRAS, 491, 2902
Fransson C., Jerkstrand A., 2015, ApJ, 814, L2
Fransson C., Kozma C., 1993, ApJ, 408, L25
García-Berro E., Althaus L. G., Córsico A. H., 2008, ApJ, 677, 473
Garstang R. H., 1958, MNRAS, 118, 234
Gough B., 2009, GNU Scientific Library Reference Manual, 3rd edn. Network Theory Ltd., USA
Hansen C. J., Wheeler J. C., 1969, Ap&SS, 3, 464
Higginbottom N., Knigge C., Long K. S., Sim S. A., Matthews J. H., 2013, MNRAS, 436, 1390
Hillebrandt W., Kromer M., Röpke F. K., Ruiter A. J., 2013, Front. Phys., 8, 116
Hillier D. J., 1990, A&A, 231, 116
Hillier D. J., Miller D. L., 1998, ApJ, 496, 407
Höflich P., Gerardy C. L., Nomoto K., Motohara K., Fesen R. A., Maeda K., Ohkubo T., Tominaga N., 2004, ApJ, 617, 1258
Hoyle F., Fowler W. A., 1960, ApJ, 132, 565
Hummer D. G., Berrington K. A., Eissner W., Pradhan A. K., Saraph H. E., Tully J. A., 1993, A&A, 279, 298
Hunter J. D., 2007, Comput. Sci. Eng., 9, 90
Iwamoto K., Brachwitz F., Nomoto K., Kishimoto N., Umeda H., Hix W. R., Thielemann F.-K., 1999, ApJS, 125, 439

Jerkstrand A., 2017, Handbook of Supernovae, Vol. 102. Springer, Berlin, p. 795
Jerkstrand A., Fransson C., Kozma C., 2011, A&A, 530, A45
Jerkstrand A., Ergon M., Smartt S. J., Fransson C., Sollerman J., Taubenberger S., Bersten M., Spyromilio J., 2015, A&A, 573, A12
Kaastra J. S., Mewe R., 1993, A&AS, 97, 443
Kasen D., Röpke F. K., Woosley S. E., 2009, Nature, 460, 869
Kerzendorf W. E., Sim S. A., 2014, MNRAS, 440, 387
Khokhlov A. M., 1991, A&A, 245, 114
Kozma C., Fransson C., 1992, ApJ, 390, 602
Kozma C., Fransson C., Hillebrandt W., Travaglio C., Sollerman J., Reinecke M., Röpke F. K., Spyromilio J., 2005, A&A, 437, 983
Kromer M., Sim S. A., 2009, MNRAS, 398, 1809
Kurucz R. L., 2006, in Ph Stee, ed., EAS Pub. Ser. Vol. 18, Radiative Transfer and Application to Very Large Telescopes, EDP Sciences, London. p. 129
Kurucz R. L., Bell B., 1995, Smithsonian Astrophysical Observatory, Kurucz CD-ROM, Cambridge, MA
Landini M., Fossi B. C. M., 1991, A&AS, 91, 183
Leung S.-C., Nomoto K., 2018, ApJ, 861, 143
Li C., Hillier D. J., Dessart L., 2012, MNRAS, 426, 1671
Liu W., Jeffery D. J., Schultz D. R., 1997, ApJ, 483, L107
Livio M., Mazzali P., 2018, Phys. Rep., 736, 1
Livne E., 1990, ApJ, 354, L53
Livne E., Glasner A. S., 1990, ApJ, 361, 244
Long K. S., Knigge C., 2002, ApJ, 579, 725
Lucy L. B., 1999, A&A, 344, 282
Lucy L. B., 2002, A&A, 384, 725
Lucy L. B., 2003, A&A, 403, 261
Lucy L. B., 2005, A&A, 429, 19
Maeda K., Taubenberger S., Sollerman J., Mazzali P. A., Leloudas G., Nomoto K., Motohara K., 2010, ApJ, 708, 1703
Maguire K. et al., 2013, MNRAS, 436, 222
Maguire K., Taubenberger S., Sullivan M., Mazzali P. A., 2016, MNRAS, 457, 3254
Marquardt K. S., Sim S. A., Ruiter A. J., Seitenzahl I. R., Ohlmann S. T., Kromer M., Pakmor R., Röpke F. K., 2015, A&A, 580, A118
Matteucci F., Greggio L., 1986, A&A, 154, 279
Maurer I., Jerkstrand A., Mazzali P. A., Taubenberger S., Hachinger S., Kromer M., Sim S. A., Hillebrandt W., 2011, MNRAS, 418, 1517
Mazzali P. A., Lucy L. B., 1993, A&A, 279, 447
Mazzali P. A., Nomoto K., Patat F., Maeda K., 2001, ApJ, 559, 1047
Mazzali P. A., Röpke F. K., Benetti S., Hillebrandt W., 2007, Science, 315, 825
Mazzali P. A., Maurer I., Stritzinger M., Taubenberger S., Benetti S., Hachinger S., 2011, MNRAS, 416, 881
Mazzali P. A. et al., 2015, MNRAS, 450, 2631
Mazzali P. A., Ashall C., Pian E., Stritzinger M. D., Gall C., Phillips M. M., Höflich P., Hsiao E., 2018, MNRAS, 476, 2905
Mazzotta P., Mazzitelli G., Colafrancesco S., Vittorio N., 1998, A&AS, 133, 403
Mewe R., 1972, A&A, 20, 215
Michel A. S., 2014, Master's thesis, Bayerische Julius-Maximilians-Universität in Würzburg
Nahar S. N., 1996, Phys. Rev. A, 53, 2417
Nahar S. N., 1997, Phys. Rev. A, 55, 1980
Nahar S. N., Bautista M. A., 2001, ApJS, 137, 201
Nahar S. N., Pradhan A. K., 1994, J. Phys. B: At. Mol. Phys., 27, 429
Nahar S. N., Bautista M. A., Pradhan A. K., 1997, ApJ, 479, 497
Nahar S. N., Bautista M. A., Pradhan A. K., 1998, Phys. Rev. A, 58, 4593
Nomoto K., Leung S.-C., 2018, Space Sci. Rev., 214, 180
Nomoto K., Thielemann F.-K., Yokoi K., 1984, ApJ, 286, 644
Opal C. B., Peterson W. K., Beaty E. C., 1971, J. Chem. Phys., 55, 4100
Pakmor R., Kromer M., Taubenberger S., Sim S. A., Röpke F. K., Hillebrandt W., 2012, ApJ, 747, L10
Perlmutter S. et al., 1999, ApJ, 517, 565
Quinet P., 1996, A&AS, 116, 573

Quinet P., Le Dourneuf M., 1996, A&AS, 119, 99
Quinet P., Le Dourneuf M., Zeippen C. J., 1996, A&AS, 120, 361
Reinecke M., Hillebrandt W., Niemeyer J. C., 2002, A&A, 386, 936
Riess A. G. et al., 1998, AJ, 116, 1009
Röpke F. K., 2005, A&A, 432, 969
Röpke F. K. et al., 2012, ApJ, 750, L19
Ruiz-Lapuente P., 1996, ApJ, 465, L83
Ruiz-Lapuente P., Lucy L. B., 1992, ApJ, 400, 127
Ruiz-Lapuente P., Kirshner R. P., Phillips M. M., Challis P. M., Schmidt B. P., Filippenko A. V., Wheeler J. C., 1995, ApJ, 439, 60
Seaton M. J., 1987, J. Phys. B: At. Mol. Phys., 20, 6363
Seitenzahl I. R., Townsley D. M., 2017, Handbook of Supernovae, Vol. 53. Springer, Berlin, p. 1955
Seitenzahl I. R. et al., 2013, MNRAS, 429, 1156
Shull J. M., van Steenberg M., 1982, ApJS, 48, 95
Sim S. A., 2007, MNRAS, 375, 154
Sim S. A., Röpke F. K., Hillebrandt W., Kromer M., Pakmor R., Fink M., Ruiter A. J., Seitenzahl I. R., 2010, ApJ, 714, L52
Sim S. A. et al., 2013, MNRAS, 436, 333

Sollerman J. et al., 2004, A&A, 428, 555
Spencer L. V., Fano U., 1954, Phys. Rev., 93, 1172
Spyromilio J., Meikle W. P. S., Allen D. A., Graham J. R., 1992, MNRAS, 258, 53P
Storey P. J., Zeippen C. J., Sochi T., 2016, MNRAS, 456, 1974
Timmes F. X., Brown E. F., Truran J. W., 2003, ApJ, 590, L83
Travaglio C., Gallino R., Arnone E., Cowan J., Jordan F., Sneden C., 2004, ApJ, 601, 864
Tyndall N. B., Ramsbottom C. A., Ballance C. P., Hibbert A., 2016, MNRAS, 462, 3350
van Regemorter H., 1962, ApJ, 136, 906
Watts M. S. T., Burke V. M., 1999, J. Phys. B: At. Mol. Phys., 31, 145
Wilk K. D., Hillier D. J., Dessart L., 2018, MNRAS, 474, 3187
Wilk K. D., Hillier D. J., Dessart L., 2019, MNRAS, preprint (arXiv:1906.01048)
Younger S. M., 1981, J. Quant. Spectrosc. Radiative Transfer, 26, 329

This paper has been typeset from a TEX/LATEX file prepared by the author.